crystals

MDPI

Article

Crystal Structure of IlvC, a Ketol-Acid Reductoisomerase, from *Streptococcus Pneumoniae*

Gyuhee Kim [1], Donghyuk Shin [1,3], Sumin Lee [2], Jaesook Yun [2] and Sangho Lee [1,*]

1 Departments of Biological Sciences, Sungkyunkwan University, 2066 Seobu-ro, Suwon 16419, Korea; khyhies77@skku.edu (G.K.); shin@med.uni-frankfurt.de (D.S.)
2 Departments of Chemistry, Sungkyunkwan University, 2066 Seobu-ro, Suwon 16419, Korea; go891209@nate.com (S.L.); jaesook@skku.edu (J.Y.)
3 Max Planck Institute of Biophysics, 60438 Frankfurt am Main, Germany
* Correspondence: sangholee@skku.edu

Received: 8 October 2019; Accepted: 23 October 2019; Published: 24 October 2019

Abstract: Biosynthesis of branched-chain amino acids (BCAAs), including isoleucine, leucine and valine, is required for survival and virulence of a bacterial pathogen such as *Streptococcus pneumoniae*. IlvC, a ketol-acid reductoisomerase (E.C. 1.1.1.86) with NADP(H) and Mg^{2+} as cofactors from the pathogenic *Streptococcus pneumoniae* (SpIlvC), catalyzes the second step in the BCAA biosynthetic pathway. To elucidate the structural basis for the IlvC-mediated reaction, we determined the crystal structure of SpIlvC at 1.69 Å resolution. The crystal structure of SpIlvC contains an asymmetric dimer in which one subunit is in apo-form and the other in NADP(H) and Mg^{2+}-bound form. Crystallographic analysis combined with an activity assay and small-angle X-ray scattering suggested that SpIlvC retains dimeric arrangement in solution and that D83 in the NADP(H) binding site and E195 in the Mg^{2+} binding site are the most critical in the catalytic activity of SpIlvC. Crystal structures of SpIlvC mutants (R49E, D83G, D191G and E195S) revealed local conformational changes only in the NADP(H) binding site. Taken together, our results establish the molecular mechanism for understanding functions of SpIlvC in pneumococcal growth and virulence.

Keywords: IlvC; *Streptococcus pneumoniae*; BCAA pathway; ketol-acid reductoisomerase

1. Introduction

Branched-chain amino acids (BCAAs), referring to isoleucine, leucine and valine, are essential amino acids in humans and are required for the survival and virulence of bacterial pathogens. The biosynthetic pathway of BCAAs is present in bacteria, algae, plants, fungi and archaea, but not in mammals, thereby rendering enzymes of this pathway to be good targets for intervention [1]. IlvX family proteins, exhibiting ketol-acid reductoisomerase (KARI; EC 1.1.1.86) activity, catalyze the second step in the BCAA pathway [2]. KARIs catalyze the conversion of acetohydroxy acids such as 2-acetolactate or 2-aceto-2-hydroxybutyrate to dihydroxy valerates including 2,3-dihydroxy-3-isovalerate or 2,3-dihydroxy-3-methylvalerate (Scheme 1) [1].

In terms of cofactor requirements, KARIs promote alkyl migration and reduction in the presence of NADP(H) and Mg^{2+} [3]. Although KARI structures from some bacteria and plants have been determined, only one structure from *Escherichia coli* is available in both apo and holo forms [4,5].

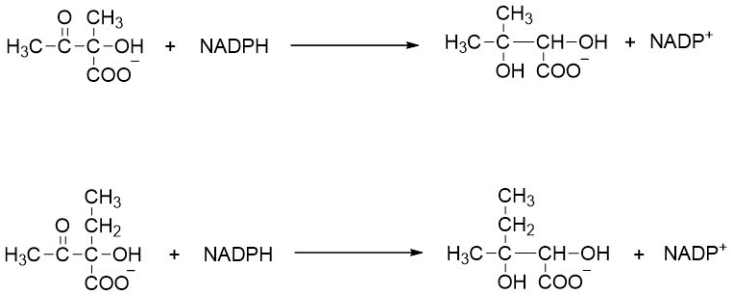

Scheme 1. Reactions catalyzed by a ketal-acid reductoisomerase.

The BCAA pathways are critical for the survival and virulence of pathogenic bacteria. For instance, the BCAA biosynthetic pathway of pathogenic *Actinobacillus pleuropneumoniae* is involved in swine pneumonia [6]. *A. pleuropneumoniae ilvI* mutant showed defects in BCAA synthesis, inhibited growth and reduced virulence in swine. Another KARI family, such as *IlvE*, a branched-chain amino acid aminotransferase, from the oral cavity pathogen *Streptococcus mutans*, is involved in acid tolerance, as well as the BCAA pathway [7].

Streptococcus pneumoniae is a pathogenic Gram-positive bacterium that is causing a global health problem [8]. This pathogen causes pneumonia, bacteraemia, meningitis, and osteomyelitis [8,9]. The *ilvC* mutant from *Streptococcus pneumoniae* reportedly leads to a reduction of its survival [10]. Despite the involvement of the *S. pneumoniae* IlvC (SpIlvC) of the BCAA pathway in pneumococcal diseases, the molecular reaction mechanism of SpIlvC is not well understood. To elucidate the structural basis of SpIlvC function, we attempted to crystallize SpIlvC. By combination of crystallographic and small-angle X-ray scattering (SAXS) analyses of the SpIlvC structure, along with biochemical activity assays, we provide a molecular framework for understanding the function of SpIlvC.

2. Materials and Methods

2.1. Materials

2.1.1. DNA Cloning and Mutagenesis

Genomic DNA of *S. pneumoniae* strain D39 was generously provided by Dong-Kwon Rhee (Sungkyunkwan University, Suwon, Republic of Korea). DNA polymerase (*Pfu* polymerase) was purchased from Solgent Inc (Daejeon, Republic of Korea); restriction enzymes (*BamH*I and *Xho*I), calf intestinal alkaline phosphatase (CIP), T4 DNA ligase, and *Dpn*I enzyme for site-directed mutagenesis were purchased from New England Biolab (Ipswitch, USA).

2.1.2. Protein Expression and Purification

Luria–Bertani (LB) medium was purchased from the USB corporation (Cleveland, OH, USA); isopropyl-1-thio-β-D-galatopyranoside (IPTG) from GeneDepot (Katy, TX, USA); Tris-HCl and NaCl from Noble BioSciences Industries (Hwaseong, Republic of Korea); imidazole from SigmaAldrich(St. Louis, MO, USA); Ni-NTA agarose resin from Qiagen (Hilden, Germany); a Superdex 200 HiLoad prep-grade column for size-exclusion chromatography from GE HealthCare (Chicago, IL, USA); and Amicon 3 kDa-centrifugal filters for concentrating protein solutions from MilliporeSigma (Burlington, NJ, USA).

2.1.3. Crystallization

Crystallization screening kits, such as Crystal Screen I/II, were purchased from Hampton Research (Aliso Viejo, CA, USA) and Wizard I/II and Cryo I/I from Molecular Dimensions (Sheffield, UK).

2.1.4. Activity Assay

2-Acetolactate was synthesized. NADPH was purchased from SigmaAldrich (St. Louis, MO, USA).

2.2. Methods

2.2.1. DNA Cloning, Protein Expression and Purification of IlvC from S. Pneumoniae

Gene encoding SpIlvC was amplified by polymerase chain reaction (PCR) using genomic DNA of the *S. pneumonaie* strain D39 as a template. The amplified DNA was digested with *BamH*I and *Xho*I. Digested DNA was inserted into the *BamHI/XhoI*-digested expression vector parallel-His2 [11], which contained a 6xHis-tag and a TEV protease recognition site. The parallel-His2-SpIlvC plasmid was transformed to *E. coli* BL21(DE3) cells for protein expression. Cells were grown at 310 K in 20 mL of LB medium supplemented with 100 µg/mL ampicillin. After 16–21 h, SpIlvC cells were transferred to 2 L of LB medium supplemented with 200 µg/mL ampicillin, and further grown at 310 K until OD_{600} reached 0.6–0.8. The cells were induced for protein expression by addition of 0.5 mM (final concentration) isopropyl-β-D-thiogalactopyranoside, and subsequently grown at 293 K for an additional 18–20 h.

The cells were harvested by centrifugation at 4000 rpm for 12 min at 277 K. The resulting cell pellets were resuspended in buffer A (50 mM Tris-HCl pH 7.5 and 150 mM NaCl), and homogenized by ultrasonication 2s/2s pulse for 30 min. Supernatant containing the soluble His_6-SpIlvC was collected by centrifugation at 13,000 rpm for 1 h at 277 K and subsequently loaded onto Ni-NTA Agarose resin. After incubating and washing with buffer B (50 mM Tris-HCl pH 7.5, 0.5 M NaCl and 20 mM imidazole), the protein was eluted in buffer C (50 mM Tris-HCl pH 7.5, 0.5 M NaCl and 0.3 M imidazole). His-tag was cleaved by GFP-TEV protease during dialysis against buffer A overnight at 277 K. The dialyzed solution supplemented with 20 mM imidazole was loaded onto Ni-NTA Agarose resin to remove the His_6-tag and GFP-TEV protease. Flow-through was collected and the cleaved SpIlvC was further purified on a Superdex-200 size-exclusion column pre-equilibrated with buffer A. Fractions containing SpIlvC were pooled and concentrated using a 3 kDa centrifugal filter. The quality of the purified SpIlvC was checked by SDS-PAGE analysis (Supplementary materials, Figure S1).

2.2.2. Site-Directed Mutagenesis

Site-directed mutagenesis was performed based on the protocol for QuikChange site-directed mutagenesis kit (Agilent). Briefly, pHis2-SpIlvC plasmid was amplified with designed mutant primers by PCR. The resulting solution was treated by addition of 1 µL *Dpn*I to remove the parental plasmid by incubation of 1.5 h at 310 K. The resulting mutant plasmid was transformed to *E. coli* strain DH5α. A single colony was inoculated in 10 mL of LB medium supplemented with 100 µg/mL ampicillin and grown at 310 K for 16–18 h. Cells were harvested by centrifugation at 4000 rpm for 12 min at 277 K. Identities of mutants were verified by DNA sequencing.

2.2.3. Crystallization

Crystallization screening for SpIlvC wild-type (WT) and its mutants was carried out by micro-batch and hanging-drop vapor-diffusion methods. Crystallization results for SpIlvC WT were described previously [12]; therefore, they are not shown in this study. Crystallization conditions of SpIlvC mutants (R49E, D83G, D191G and E195S) are summarized in Table 1.

Table 1. Crystallization conditions of SpIlvC mutants.

Parameter	R49E	D83G	D191G	E195S
Method Plate type	**Hanging Drop Vapor Diffusion** **24-Well Plate**			
Temperature (K)	288	295	288	295
Protein concentration	8.2 mg mL^{-1}	9 mg mL^{-1}	12 mg mL^{-1}	7.25 mg mL^{-1}
Buffer composition of protein solution	50 mM Tris-HCl pH 7.5, 150 mM NaCl	50 mM Tris-HCl pH 7.5, 150 mM NaCl	50 mM Tris-HCl pH 7.5, 150 mM NaCl	50 mM Tris-HCl pH 7.5, 150 mM NaCl
Composition of reservoir solution	0.1 M HEPES pH 7.5, 0.1 M NaCl, 1.8 M ammonium sulfate, 25% glycerol	0.1 M HEPES pH 7.5, 0.1 M NaCl, 1.8 M ammonium sulfate	0.1M HEPES pH 7.5, 0.1 M NaCl, 1.5 M ammonium sulfate, 15% glycerol	0.1 M Tris-HCl pH 8.0, 0.1 M NaCl, 1.6 M ammonium sulfate
Volume and ratio of drop	1 µL protein solution with 1 µL reservoir solution	1 µL protein solution with 1 µL reservoir solution	1 µL protein solution with 1 µL reservoir solution	1 µL protein solution with 1 µL reservoir solution
Volume of reservoir	500 µL	500 µL	500 µL	500 µL

2.2.4. Crystallographic Data Processing and Structure Determination

Dagger-shaped crystals appeared in 3–5 days. The crystals were transferred to a cryoprotectant solution containing 30% glycerol. Diffraction data were collected on a single frozen crystal in a 100 K gaseous nitrogen stream over a range of 360° with a rotation angle per image of 1.0° at beamlines 5C and 7A in Pohang Accelerator Laboratory, Korea. Data processing and reduction were carried out using *HKL-2000* [13]. The data collection and processing statistics are summarized in Table 2. For phasing by molecular replacement (MR), an MR solution was found using *PHENIX* [14] with a KARI from *Pseudomonas aeruginosa* sharing 54% sequence identity (PDB code: 1NP3) as a search model. Iterative model building and refinement were done using *PHENIX* and *COOT* [15]. Diffraction data and coordinates have been deposited to the protein data bank with identification codes 6L2I (WT), 6L2K (R49E), 6L2S (D83G), 6L2Z (D191G) and 6L2R (E195S).

Table 2. Structure refinement statistics.

Parameter	WT	R49E	D83G	D191G	E195S
Diffraction source	PAL 7A				
Resolution range (Å)	41.63–1.69 (1.75–1.69)*	26.81–1.95 (2.02–1.95)	30.3–2.29 (2.37–2.29)	23.87–2.02 (2.09–2.02)	43.43–2.02 (2.1–2.02)
Space group	$P2_12_12_1$	$P2_12_12_1$	$P2_1$	$P2_12_12_1$	$P2_12_12_1$
Cell axis (Å)	69.1, 104.3, 110.9	69.5, 104.1, 111.0	71.9, 68.5, 81.2,	68.9, 104.5, 112.5	69.1, 104.4, 111.6
Cell angle (°)	90, 90, 90	90, 90, 90	90, 95, 90	90, 90, 90	90, 90, 90
Completeness (%)	98.98 (98.87)	96.1 (97.9)	99.8 (100)	98.1(100)	99.8 (97.0)
σ cut-off	0	0	0	0	0
No. of reflections, working set	86927 (8538)	54008 (5172)	33561 (3244)	49986 (4989)	50411 (4895)
No. of reflections, test set	2008 (201)	2898 (284)	1760 (170)	2686(277)	2696 (257)
Final R_{cryst}	0.191	0.204	0.159	0.204	0.179
Final R_{free}	0.206	0.244	0.212	0.242	0.219
No. of non-Hatoms					
Protein	5055	5061	9941	5413	5007
Ion	26	21	40	15	24
Ligand	90	-	-	108	96
Water	696	485	277	552	433
Total	5867	5567	10258	5818	5560
R.m.s. deviations					
Bonds (Å)	0.007	0.009	0.008	0.009	0.0076
Angles (°)	1.09	1.10	1.08	1.18	1.12
Average *B* factors (Å^2)					
Protein	30.1	60.9	34.7	33.4	31.5
Ion	11.3	9.73	14.1	10.7	15.6
Ligand	16.2	-	-	1.72	1.13
Water	42.4	37.3	37.2	41.3	38.6
Ramachandran plot					
Most favoured (%)	96.41	96.05	97	97.69	96.8
Allowed (%)	3.59	3.34	3	2.31	3.08

*Values for the outer shell are given in parentheses.

2.2.5. Reductase Activity Assay

2-Acetolactate (5.9 mM solution), a substrate, was prepared by basic hydrolysis of its *O*-acetyl ethyl ester according to the procedures described in [16,17] and stored at −20 °C. The reaction scheme of 2-Acetolactate is described in Supplementary Figure S2. SpIlvC (1 µM) was pre-incubated in the activity assay buffer (50 mM Tris-HCl pH 8.0, 10 mM $MgCl_2$, and 350 µM NADP(H)) at 30 °C for 20 min. After pre-incubation, the 0 to 1.24 mM substrate was added to the reaction mixture and decrease in the absorbance at 340 nm was monitored on a spectrophotometer (GE HealthCare). The absorbance at 340 nm reflects the change in the concentration of NADP(H). K_m values were determined using the Michaelis–Menten equation.

2.2.6. Small-Angle X-Ray Scattering (SAXS) Measurement, Data Processing and Validation

Purified IlvC protein was concentrated to 2.94 mg/mL in buffer A, and SAXS data were obtained at beamline 4C at the Pohang Accelerator Laboratory, Korea. Buffer A was measured for subtraction of the buffer. Serially diluted (three-, nine-fold) samples were measured to ensure concentration-independent behavior of the sample in solution. The 1D SAXS profile was obtained by a home-made program at beamline 4C. The final SAXS profile was generated by merging a low-concentration profile with that of a high-concentration sample by *PRIMUS* [18]. The Guinier region is analyzed by *AUTORG*, and the pair distribution function ($P(r)$), D_{max}, and Porod volume were calculated by *AUTOGNOM* [19]. To avoid the ambiguity of ab initio shape determination, ten different models were generated by *DAMMIF* [20] and analyzed by *DAMAVER* to select the best model [21]. The best model—the one with the lowest NSD—was chosen for the final molecular envelope model for IlvC. The comparison of the experimental data with the calculated scattering profile of the crystal structure was performed by the *FoXS* server [22,23]. SAXS data processing and refinement statistics are summarized in Table 3.

Table 3. Small-angle X-ray scattering data processing and analysis statistics.

Parameter	SpIlvC WT
Data collection parameters	
Synchrotron beamline	PAL 4C
Beam geometry	Mica window solid cell/Oscillation capillary
Wavelength (Å)	1.24
Exposure time (min)	0.5
Concentration range (mg mL^{-1})	2.94
Sample parameters	
Polydispersity (%, by DLS)	9.45
Structural parameters	
$I(0)$ (cm^{-1}) [from Guinier]	7064.9 ± 16.2
R_g (Å) [from Guinier]	27.5 ± 0.1
$I(0)$ (cm^{-1}) [from $P(r)$]	7160
R_g (Å) [from $P(r)$]	27.9
D_{max} (Å)	85.8
Porod volume estimate (Å)	100470
Software employed	
Primary data reduction	*In-house program at PAL 4C*
Data processing	*PRIMUS*
Ab initio analysis	*DAMMIF/DAMMIN*
Validation and averaging	*CRYSOL*
Three-dimensional representations	*PyMOL*

3. Results

3.1. SpIlvC Reveals an Asymmetric Dimer in the Crystal

We determined the crystal structure of SpIlvC WT at a resolution of 1.69 Å. Known plant and bacterial KARI structures are reportedly categorized as classes I and II [24]. The SpIlvC structure corresponds to a class I KARI protein from Gram-positive bacteria (Supplementary Table S1). The crystal of SpIlvC contained two molecules in the asymmetric unit, consistent with homologous KARIs being dimers (Figure 1a). Interestingly, we found electron density for NADP(H) in one protomer, although we did not include NADP(H) in the crystallization conditions (Figure 1b). We infer that the NADP(H) molecule may have originated from *E. coli* cytoplasm. Subsequent refinement revealed that one protomer contained both magnesium ions and NADP(H), thereby constituting an asymmetric dimer in the crystal. This is in contrast to the observation that most bacterial and plant KARI structures have artificially added co-factors [25–28].

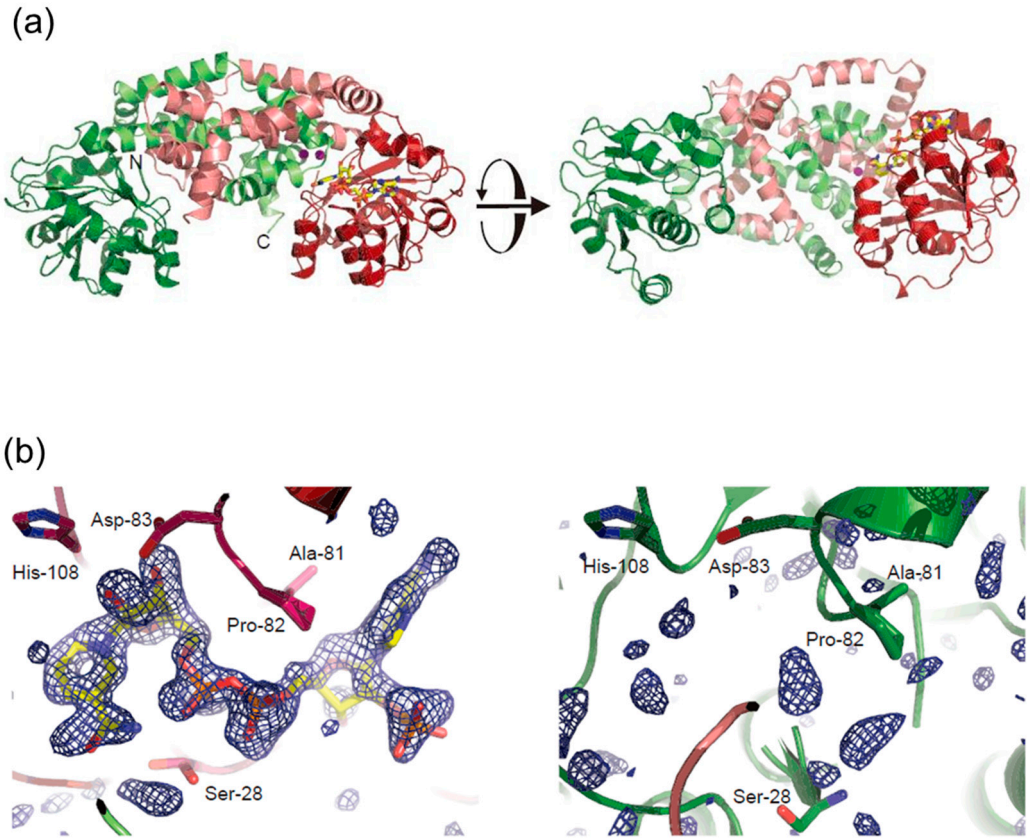

Figure 1. The crystal structure of SpIlvC, featuring an asymmetric dimer. **(a)** The SpIlvC structure contains an asymmertic dimer. One protomer in apo form is colored green and the other protomer in holo form with NADP(H) and bound Mg^{2+} is colored in red. N-terminal domains are dark-colored, while C-terminal domains light-colored. NADP(H) is shown as stick models. Mg^{2+} is depicted as purple spheres. The two views are related by a 90° rotation. **(b)** A stimulated omit map contoured 1σ surrounding the NADP(H) binding site of two protomers is shown. (*Left*) NADP(H) is well fitted to the electron density. (*Right*) The same NADP(H) binding site of the other protomer exhibits no suitable density for NADP(H).

3.2. Comparison of Apo and Cofactor-Bound Structures

The overall conformation of SpIlvC remains the same regardless of the presence of cofactors such as NAPDH and Mg^{2+}, as evidenced by an root mean square deviation (r.m.s.d.) of Cα atoms between the apo and holo forms of 1.0 Å. Superposition of the structures of two protomers showed larger local

conformation changes in the N-terminal domain harbouring the NADP(H) binding site than in the C-terminal domain (Figure 2a). A residue-level r.m.s.d. comparison revealed that residues 50–60, corresponding to the α2 helix of the β2α2 loop showed the largest r.m.s.d. (Figure 2b). KARIs harbor a GxGxxG motif, which is part of the nucleotide binding site by phosphate-bridging interaction [24]. Ser-28 in the GxGxxG loop contacting NADP(H), exhibits a large r.m.s.d. (Figure 2b), consistent with the idea that cofactor binding causes local conformational changes [29]. These results suggest that the N-terminal domain of SpIlvC undergoes large local conformational changes upon NADP(H) and Mg^{2+} binding.

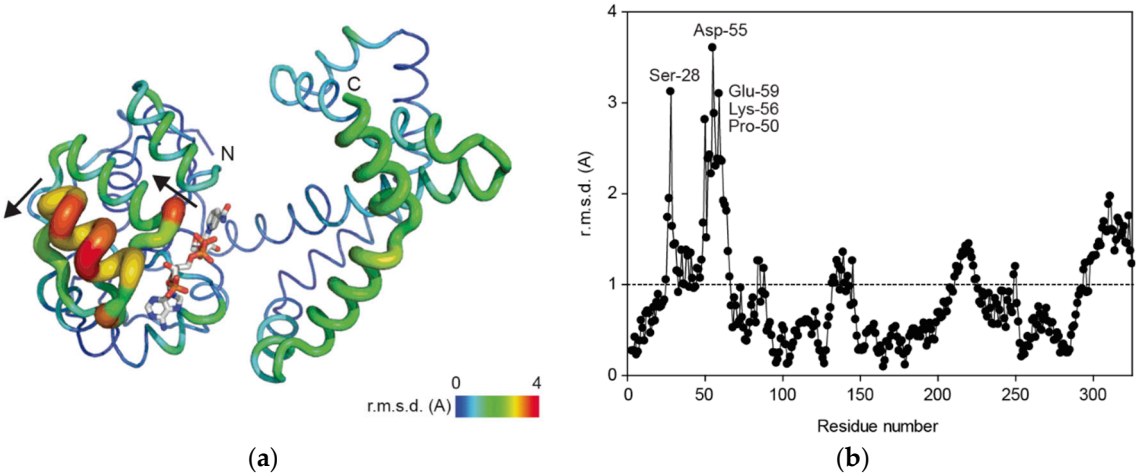

(**a**) (**b**)

Figure 2. Comparison of two protomers in the SpIlvC crystal structure. **(a)** R.m.s.d. values between the two protomers are shown as a color spectrum. Arrows indicate the direction of local conformational changes. NADP(H) is depicted as stick models and SpIlvC as ribbon representations. **(b)** Residue-by-residue r.m.s.d. between the two protomers (chain A and B). Residues with r.m.s.d. larger than 2.5 Å are labeled.

3.3. Structures of Active-Site Mutants

Analysis of residues contacting NADP(H) and Mg^{2+} identified five amino acid residues as contacting ones: Arg-49, Asp-83, Ser-53, Asp-191, and Glu-195 (Figure 3a). Structure-based multiple sequence alignment of SpIlvC and KARIs from bacteria and plants with known structures revealed that residues contacting both NADP(H) and Mg^{2+} are conserved, while the overall length of each KARI is different (Supplementary Figure S3). Since IlvC and its orthologous proteins have either reductase or isomerase activity [4], we determined the reductase activity of SpIlvC wild-type (WT) and its active-site mutants. Enzymatic activity of SpIlvC was determined by monitoring the decrease of absorbance at 340 nm characteristic of NADP(H) [4]. To investigate the effects of charge and size of the side chains of active-site residues on the kinetics of SpIlvC, we prepared 13 mutants in five residues: R49G, R49A, and R49E; S53G, S53A, S53T, and S53K; D83G; D191G and D191K; and E195A, E195S, and E195K. All the mutants exhibited significantly reduced activities compared to that of WT (Figure 3b), corroborating the structural analysis. Kinetic parameters for SpIlvC WT and mutants are summarized in Table 4. Representative kinetic data for SpIlvC WT and selected mutants (R49E, D83G, D191G and E195S) are shown in Supplementary Figure S4. The reductase activity of SpIlvC is comparable to those of *E. coli* KARI and a *Methanococcus aeolicus* KARI mutant [25].

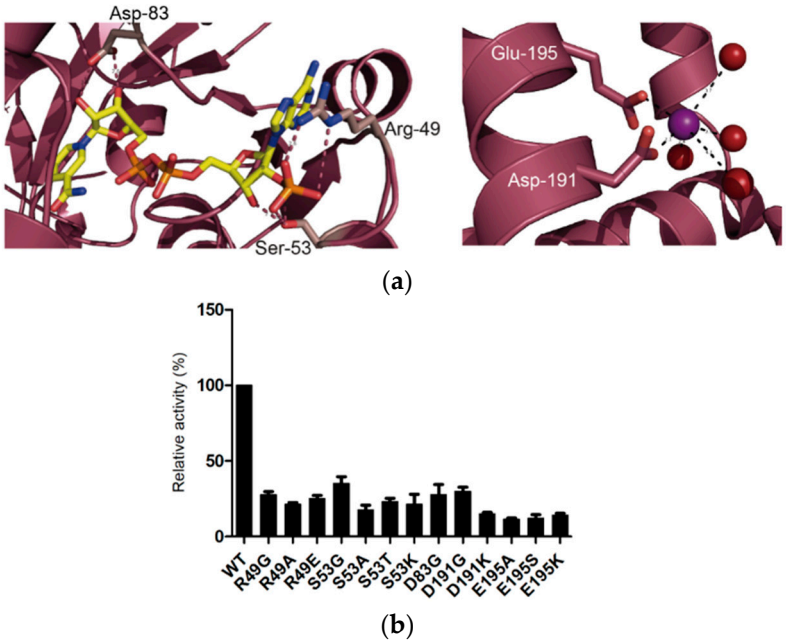

Figure 3. Analysis of active-site residues of SpIlvC. **(a)** Structure of NADP(H) and Mg^{2+} binding sites. (*Left*) NADP(H) (stick models) binding is mediated by Arg-49, Ser-53, and Asp-83. (*Right*) Mg^{2+} (magenta sphere) coordination is mediated by Asp-191 and Glu-195. Distances are shown in Å. Water molecules are depicted as red spheres. Side chains of the residues are represented as stick models. **(b)** Relative catalytic activities of SpIlvC wild-type (WT) and its mutants. The relative activities and standard deviation of the mutants in reference to those of WT are shown. The enzymatic activity of WT was set to 1.0.

Table 4. Kinetic parameters of SpIlvC wild-type and its mutants.

Mutant	K_M (μM)	k_{cat} (s^{-1})	k_{cat}/K_M ($\mu M^{-1}s^{-1}$)[a]
WT	70 ± 1.21	0.10 ± 0.01	1.4×10^{-3}
R49G	395 ± 57	0.16 ± 0.01	4.3×10^{-4}
R49A	588 ± 194	0.18 ± 0.01	3.0×10^{-4}
R49E	472 ± 134	0.18 ± 0.02	3.8×10^{-4}
S53G	199 ± 34	0.11 ± 0.02	5.5×10^{-4}
S53A	677 ± 61	0.17 ± 0.02	2.5×10^{-4}
S53T	345± 83	0.12 ± 0.01	3.4×10^{-4}
S53K	471 ± 29	0.14 ± 0.02	3.0×10^{-4}
D83G	330 ± 37	0.13 ± 0.03	3.9×10^{-4}
D191G	355 ± 44	0.15 ± 0.01	4.2×10^{-4}
D191K	1036 ± 298	0.22 ± 0.02	2.1×10^{-4}
E195A	732 ± 201	0.12 ± 0.01	1.6×10^{-4}
E195S	1467 ± 142	0.25 ± 0.03	1.7×10^{-4}
E195K	895 ± 185	0.18 ± 0.01	2.0×10^{-4}

[a]The values are for NADP(H).

To obtain further structural details on the roles of active-site residues, we determined crystal structures of five mutants: two NADP(H) binding-site mutants (R49E and D83G) and two Mg^{2+} binding-site mutants (D191K and E195S) at resolutions ranging from 1.7 Å to 2.3 Å (Table 2). Superposition of structures of WT and NADP(H) binding-site mutants, such as R49E and D83G, revealed rotameric changes in residues His-31, Lys-52, Phe-54, and His-135 (Figure 4a,b). By contrast, structures of Mg^{2+} binding-site mutants, such as D191G and E195S, showed no change in rotamers of the corresponding residues in the structure of WT (Figure 4c,d). These results suggested that bulky

residues in the NADP(H) binding site move to the outward positions, resulting in the NADP(H) binding pocket broadening through rotameric changes. The NADP(H) site mutants are likely to bind to NADP(H) weakly.

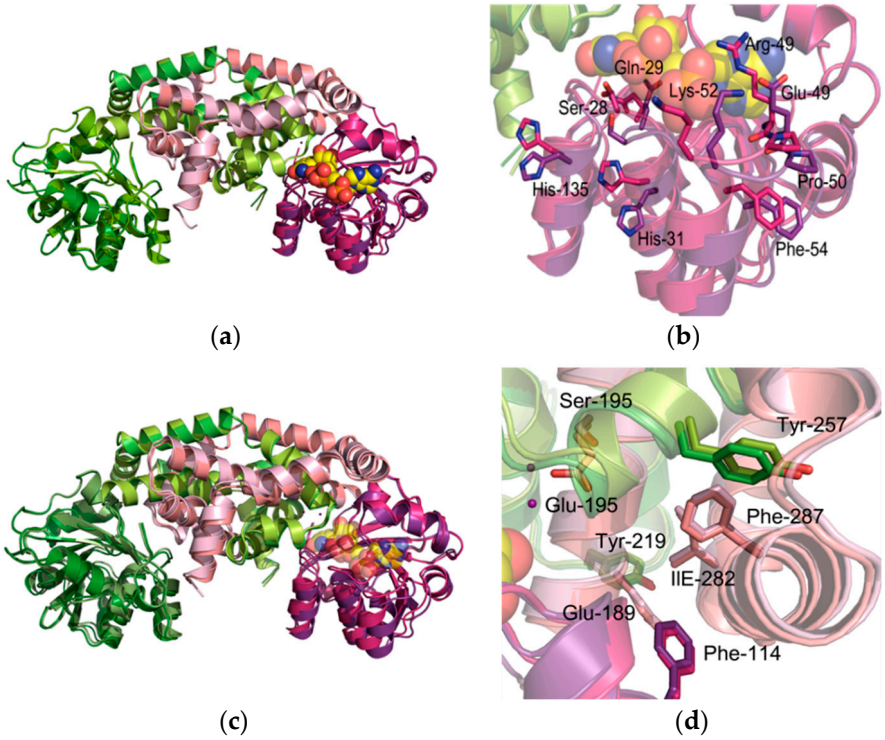

Figure 4. Superposition of the structures of WT and mutants R49E and E195S. **(a)** Superposition of the crystal structures of WT and NADP(H) binding-site mutant R49E (r.m.s.d. of Cα atoms being 0.274 Å). One protomer in the apo form is colored as green and lime for the N-terminal domain of WT and R49E, respectively; as pale green and pale lime for the C-terminal domain of WT and R49E, respectively. The other protomer in the holo form is colored as pink and purple for the N-terminal domain of WT and R49, respectively; as pale pink and pale purple for the C-terminal domain of WT and R49E, respectively. NADP(H) is depicted as stick models. **(b)** Superposition of the NADP(H) binding sites of WT (pink) and R49E (purple). Rotameric changes are observed in the following residues: His-31, Lys-52, Phe-54, and His-135. **(c)** Superposition of the crystal structures of WT and Mg^{2+} binding-site mutant E195S (r.m.s.d. of Cα atoms being 0.760 Å). The coloring scheme is the same as the panel **a**. **(d)** Superposition of the Mg^{2+} binding sites of WT (pale pink) and E195S (pale purple). No rotameric changes are observed in the Mg^{2+} binding residues.

3.4. Solution Behaviour of SpIlvC

The crystal structure of SpIlvC revealed an asymmetric dimer (Figure 1a). To investigate the solution structure, we employed a small-angle X-ray scattering (SAXS) method. The radius of gyration (R_g) and maximal distance (D_{max}) of SpIlvC in solution were estimated to be 27.5 Å and 85.8 Å, respectively (Figure 5a,b), which were both consistent with the values derived from the crystal structure-R_g being 27.6 Å andsupple D_{max} being 89 Å. Comparison of the experimental solution scattering curve with the calculated one based on the crystal structure revealed a χ^2 value of 1.57 (Figure 5c). The ab initio molecular envelope derived from SAXS data appears to be well matched with the crystal structure (Figure 5d). These results support that conformation of SpIlvC remains consistent both in crystalline and solution states.

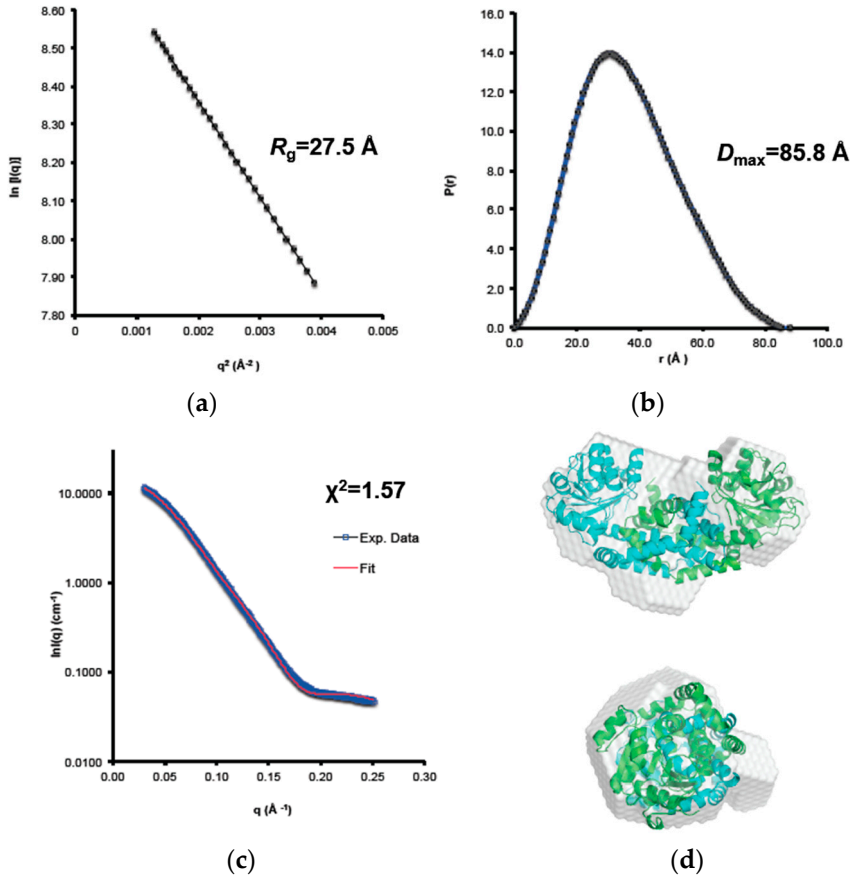

Figure 5. Small-angle X-ray scattering (SAXS) analysis of SpIlvC. **(a)** Guinier plot. **(b)** Pair distance distribution function, $P(r)$. **(c)** Fitting of the experimental scattering curve with the curve calculated from the crystal structure. The χ^2 value is 1.57. **(d)** An ab initio molecular envelope derived from SAXS data. The envelope was fitted with the crystal structure represented as ribbons.

4. Discussion

We determined the crystal structures of SpIlvC wild-type and mutants to investigate the mechanistic aspects of the function of SpIlvC. The SpIlvC crystal contains an asymmetric dimer where one protomer is in the holo form, bound by cofactors such as Mg^{2+} and NADP(H), while the other is in the apo form (Figure 1). Since we did not intend to co-crystallize SpIlvC with cofactors, these ligand molecules appear to have originated from *E. coli* cytoplasm during expression [30]. An unnatural asymmetric dimer is not unprecedented. Unlike our structure, for other structures of KARI in complex with the cofactors, the cofactors are found in all subunits (Supplementary Table S1). Small-angle X-ray light scattering (SAXS) analysis of SpIlvC demonstrated that the structure of SpIlvC is consistent in both crystalline and solution states (Figure 5). The SAXS-derived molecular envelope does not clarify whether SpIlvC retains the asymmetric dimer, as observed in the crystal unambiguously. Nevertheless, our structure provides a rather less-represented case of an asymmetric dimer observed in a crystal.

Local conformational changes can affect the catalytic activity and cofactor binding of an enzyme. KARIs have a GxGxx(G/A)xxx(G/A) motif as a binding site for NADP(H), and Mg^{2+} is required for binding NADP(H) [3,5,25]. Structure-based multiple-sequence alignment of KARIs showed that residues constituting NADP(H) and Mg^{2+} binding sites are well conserved, while the overall length of each KARI protein is different (Supplementary Figure S3). Comparative analysis of the crystal structures of the NADP(H) binding-site mutants (R49E and D83G) and Mg^{2+} binding-site mutants (D191G and E195S) uncovered that local conformational changes are observed only in the NADP(H) binding site (Figure 4b)—His-31, Lys-52, Phe-54 and His-135—and not in the Mg^{2+} binding one (Figure 4d). These results implicate that differential rotameric changes would occur in the NADP(H)

binding sites only, despite the similar detrimental effects by mutations in both NADP(H) and Mg^{2+} binding-site residues on the catalytic activity of SpIlvC.

BCAA biosynthesis is critical for survival and virulence of pneumococcal pathogens. A small amount of essential BCAA exists in a healthy pig lung and *A. pleuropneumoniae*, a respiratory pathogen causing swine pneumonia, seems to be responsible for such a low level of BCAA [6]. The *ilvI* mutant of *A. pleuropneumoniae* inhibits growth of the pathogen in respiratory swine. A recent physiological study reported that *ilvC* mutant induced defects in the BCAA pathway in *S. pneumoniae* [10]. The defective *ilvC* mutant of *S. pneumoniae* leads to reduced cell growth and colonization, and to increased survival of the infected rats. Given the biological and pathological importance of pneumococcal enzymes in the BCAA biosynthesis, our study discloses the mechanistic aspects of the functioning of IlvC and thereby, can serve as a starting point for understanding the effects of SpIlvC on pneumococcal virulence and physiology.

Supplementary Materials: The following are available online at http://www.mdpi.com/2073-4352/9/11/551/s1, Table S1: Known KARI structures, Figure S1: Synthesis scheme of 2-acetolactate, and Figure S2: Structure-based multiple sequence alignment of SpIlvC with KARIs from other organisms.

Author Contributions: Conceptualization, S.L.; methodology, G.K., D.S., S.L., J.Y., S.L.; formal analysis, G.K., D.S., S.L.; writing—original draft preparation, G.K., S.L.; writing—review and editing, G.K., S.L.; visualization, G.K., S.L.; supervision, S.L.; project administration, S.L.; funding acquisition, S.L.

Funding: This research was supported by the Next-Generation BioGreen 21 program (PJ01367602) through the Rural Development Administration and the Basic Science Research Program (NRF-2018R1A2B6004367 and NRF-2019R1A6A7076041) and the Science Research Center Program (SRC-2017R1A5A1014560) through the National Research Foundation of Korea (NRF) grants.

Acknowledgments: We thank staff members at beamlines 4C and 7A at the Pohang Accelerator Laboratory for technical assistance in SAXS and crystallographic data collection, and Dong-Kwon Rhee for generously providing us with genomic DNA of *S. pneumoniae*.

Conflicts of Interest: The authors declare no conflict of interest. The funders had no role in the design of the study; in the collection, analyses, or interpretation of data; in the writing of the manuscript, or in the decision to publish the results.

Abbreviations

BCAA, branched-chain amino acid; KARI, ketol-acid reductoisomerase; and SAXS, small-angle X-ray scattering.

References

1. McCourt, J.A.; Duggleby, R.G. Acetohydroxyacid synthase and its role in the biosynthetic pathway for branched-chain amino acids. *Amino Acids* **2006**, *31*, 173–210. [CrossRef] [PubMed]
2. Grandoni, J.A.; Marta, P.T.; Schloss, J.V.; Le Pocher, H.; Brouqui, P.; Raoult, D. Inhibitors of branched-chain amino acid biosynthesis as potential antituberculosis agents. *J. Antimicrob. Chemother.* **1998**, *42*, 475–482. [CrossRef]
3. Dumas, R.; Biou, V.; Halgand, F.; Douce, R.; Duggleby, R.G. Enzymology, structure, and dynamics of acetohydroxy acid isomeroreductase. *Acc. Chem. Res.* **2001**, *34*, 399–408. [CrossRef] [PubMed]
4. Tyagi, R.; Lee, Y.T.; Guddat, L.W.; Duggleby, R.G. Probing the mechanism of the bifunctional enzyme ketol-acid reductoisomerase by site-directed mutagenesis of the active site. *FEBS J.* **2005**, *272*, 593–602. [CrossRef] [PubMed]
5. Wong, S.-H.; Lonhienne, T.G.; Winzor, D.J.; Schenk, G.; Guddat, L.W. Bacterial and Plant Ketol-Acid Reductoisomerases Have Different Mechanisms of Induced Fit during the Catalytic Cycle. *J. Mol. Biol.* **2012**, *424*, 168–179. [CrossRef] [PubMed]
6. Subashchandrabose, S.; Leveque, R.M.; Wagner, T.K.; Kirkwood, R.N.; Kiupel, M.; Mulks, M.H. Branched-Chain Amino Acids Are Required for the Survival and Virulence of Actinobacillus pleuropneumoniae in Swine. *Infect. Immun.* **2009**, *77*, 4925–4933. [CrossRef] [PubMed]
7. Santiago, B.; MacGilvray, M.; Faustoferri, R.C.; Quivey, R.G. The Branched-Chain Amino Acid Aminotransferase Encoded by ilvE Is Involved in Acid Tolerance in Streptococcus mutans. *J. Bacteriol.* **2012**, *194*, 2010–2019. [CrossRef]

8. Kadioglu, A.; Weiser, J.N.; Paton, J.C.; Andrew, P.W. The role of Streptococcus pneumoniae virulence factors in host respiratory colonization and disease. *Nat. Rev. Microbiol.* **2008**, *6*, 288–301. [CrossRef]
9. Weiser, J.N.; Ferreira, D.M.; Paton, J.C. Streptococcus pneumoniae: Transmission, colonization and invasion. *Nat. Rev. Microbiol.* **2018**, *16*, 355–367. [CrossRef]
10. Kim, G.-L.; Lee, S.; Luong, T.T.; Nguyen, C.T.; Park, S.-S.; Pyo, S.; Rhee, D.-K. Effect of decreased BCAA synthesis through disruption of ilvC gene on the virulence of Streptococcus pneumoniae. *Arch. Pharmacal Res.* **2017**, *40*, 921–932. [CrossRef]
11. Sheffield, P.; Garrard, S.; Derewenda, Z. Overcoming Expression and Purification Problems of RhoGDI Using a Family of "Parallel" Expression Vectors. *Protein Expr. Purif.* **1999**, *15*, 34–39. [CrossRef] [PubMed]
12. Gyuhee Kim, S.L. Crystallization and preliminary crystallographic analysis of IlvC, a ketol-acid reductoisomerase, from Streptococcus pneumoniae D39. *Biodesign* **2017**, *1*, 89–92.
13. Otwinowski, Z.; Minor, W. Processing of X-ray diffraction data collected in oscillation mode. *Methods Enzymol.* **1997**, *276*, 307–326. [PubMed]
14. Adams, P.D.; Afonine, P.V.; Bunkóczi, G.; Chen, V.B.; Davis, I.W.; Echols, N.; Headd, J.J.; Hung, L.-W.; Kapral, G.J.; Grosse-Kunstleve, R.W.; et al. PHENIX: A comprehensive Python-based system for macromolecular structure solution. *Acta Crystallogr. Sect. D Biol. Crystallogr.* **2010**, *66*, 213–221. [CrossRef]
15. Emsley, P.; Lohkamp, B.; Scott, W.G.; Cowtan, K. Features and development of Coot. *Acta Crystallogr. Sect. D Biol. Crystallogr.* **2010**, *66*, 486–501. [CrossRef]
16. Lawrence, M.; Sayre, F.R.J. Novel Decarboxylative Oxidation of -Hydroxy-jS-keto (or -/3-imino) Acid Salts of Mercury(II). *J. Org. Chem.* **1978**, *43*, 4700–4705.
17. Krampitz, L.O. Synthesis of alpha-acetolactic acid. *Arch. Biochem.* **1948**, *17*, 81–85.
18. Konarev, P.V.; Volkov, V.V.; Sokolova, A.V.; Koch, M.H.J.; Svergun, D.I. PRIMUS: A Windows PC-based system for small-angle scattering data analysis. *J. Appl. Crystallogr.* **2003**, *36*, 1277–1282. [CrossRef]
19. Svergun, D.I. Determination of the regularization parameter in indirect-transform methods using perceptual criteria. *J. Appl. Crystallogr.* **1992**, *25*, 495–503. [CrossRef]
20. Franke, D.; Svergun, D.I. DAMMIF, a program for rapid ab-initio shape determination in small-angle scattering. *J. Appl. Crystallogr.* **2009**, *42*, 342–346. [CrossRef]
21. Volkov, V.V.; Svergun, D.I. Uniqueness of ab initio shape determination in small-angle scattering. *J. Appl. Crystallogr.* **2003**, *36*, 860–864. [CrossRef]
22. Schneidman-Duhovny, D.; Hammel, M.; Sali, A. FoXS: A web server for rapid computation and fitting of SAXS profiles. *Nucleic Acids Res.* **2010**, *38*, W540–W544. [CrossRef] [PubMed]
23. Schneidman-Duhovny, D.; Hammel, M.; Tainer, J.A.; Sali, A. Accurate SAXS Profile Computation and its Assessment by Contrast Variation Experiments. *Biophys. J.* **2013**, *105*, 962–974. [CrossRef] [PubMed]
24. Tyagi, R.; Duquerroy, S.; Navaza, J.; Guddat, L.W.; Duggleby, R.G. The crystal structure of a bacterial Class II ketol-acid reductoisomerase: Domain conservation and evolution. *Protein Sci.* **2005**, *14*, 3089–3100. [CrossRef]
25. Brinkmann-Chen, S.; Flock, T.; Cahn, J.K.; Snow, C.D.; Brustad, E.M.; McIntosh, J.A.; Meinhold, P.; Zhang, L.; Arnold, F.H. General approach to reversing ketol-acid reductoisomerase cofactor dependence from NADPH to NADH. *Proc. Natl. Acad. Sci. USA* **2013**, *110*, 10946–10951. [CrossRef]
26. Brinkmann-Chen, S.; Cahn, J.; Arnold, F. Uncovering rare NADH-preferring ketol-acid reductoisomerases. *Metab. Eng.* **2014**, *26*, 17–22. [CrossRef]
27. Ahn, H.J.; Eom, S.J.; Yoon, H.-J.; Lee, B.I.; Cho, H.; Suh, S.W. Crystal Structure of Class I Acetohydroxy Acid Isomeroreductase from Pseudomonas aeruginosa. *J. Mol. Biol.* **2003**, *328*, 505–515. [CrossRef]
28. Biou, V.; Dumas, R.; Cohen-Addad, C.; Douce, R.; Job, D.; Pebay-Peyroula, E. The crystal structure of plant acetohydroxy acid isomeroreductase complexed with NADPH, two magnesium ions and a herbicidal transition state analog determined at 1.65 A resolution. *EMBO J.* **1997**, *16*, 3405–3415. [CrossRef]
29. Kufareva, I.; Abagyan, R. Methods of protein structure comparison. *Breast Cancer* **2012**, *857*, 231–257.
30. Dai, X.; Li, Y.; Meng, G.; Yao, S.; Zhao, Y.; Yu, Q.; Zhang, J.; Luo, M.; Zheng, X. NADPH Is an Allosteric Regulator of HSCARG. *J. Mol. Biol.* **2009**, *387*, 1277–1285. [CrossRef]